Mars' ionospheric interaction with comet C/2013 A1 Siding-Spring's coma at their closest approach as seen by Mars Express

Beatriz Sánchez-Cano[1], Mark Lester[1], Olivier G. Witasse[2], David, DeWitt Morgan[3], Hermann Opgenoorth[4], David, J Andrews[5], Pierre-Louis Blelly[6], Stanley, W. H. Cowley[1], Andrew, J. Kopf[3], Francois Leblanc[7], and Jared, Randolph Espley[8]

[1]University of Leicester
[2]ESA / ESTEC
[3]University of Iowa
[4]Department of Physics, Umeå University
[5]Swedish Institute for Space Physics (IRF)
[6]Institut de Recherche en Astrophysique et Planétologie
[7]LATMOS/CNRS, Sorbonne Université, UVSQ, IPSL
[8]NASA Goddard

November 21, 2022

Abstract

On 19 October 2014, Mars experienced a very close encounter with Comet C/2013 A1 Siding Spring. Using data from the Mars Advanced Radar for Subsurface and Ionosphere Sounding (MARSIS) on board Mars Express (MEX), we assess the interaction of the Martian ionosphere with the comet's atmosphere and possibly magnetic tail during the orbit of their closest approach. The topside ionospheric electron density profile is evaluated from the peak density of the ionosphere to the local plasma around Mars Express. We find unusual, complex and rapid variability in the ionospheric profile along the MEX orbit, not seen even after the impact of large coronal mass ejections. Before closest approach, large electron density reductions predominate, which could be caused either by comet water-damping, or comet magnetic field interactions. After closest approach, a substantial electron density rise predominates. Moreover, several extra topside layers are visible along the whole orbit at different altitudes, which could be related to different processes as we discuss.

Mars' ionospheric interaction with comet C/2013 A1 Siding-Spring's coma at their closest approach as seen by Mars Express

Beatriz Sánchez–Cano[1], Mark Lester[1], Olivier Witasse[2], David D. Morgan[3], Hermann Opgenoorth[4,1], David J. Andrews[5], Pierre-Louis Blelly[6], Stanley W.H. Cowley[1], Andy Kopf[3], Francois Leblanc[7], Jared R. Espley[8]

[1] Radio and Space Plasma Physics Group, Department of Physics and Astronomy, University of Leicester, University Road, Leicester, LE1 7RH, UK.

[2] European Space Agency, ESTEC – Scientific Support Office, Keplerlaan 1, Noordwijk 2200 AG, The Netherlands.

[3] Department of Physics and Astronomy, University of Iowa, Iowa City, IA, USA

[4] Department of Physics, Umeå University, Linnaeus väg 24, 901 87 Umea, Sweden

[5] Swedish Institute of Space Physics, Uppsala, Sweden

[6] Institut de Recherche en Astrophysique et Planétologie (IRAP), Toulouse, France.

[7] LATMOS/CNRS, Sorbonne Université, UVSQ, Paris, France

[8] NASA Goddard Space Flight Center, Greenbelt, Maryland, USA

Corresponding author: Beatriz Sánchez-Cano (bscmdr1@leicester.ac.uk)

Key Points:

- We analyze the Mars Express-MARSIS observations of the interaction between Mars' ionosphere and comet Siding Spring at closest approach
- Large Martian ionospheric variability is observed during the closest approach with comet Siding-Spring
- Cometary water, dust and comet induced magnetic field seem to be equally responsible for the large ionospheric density variability

Key Words: ionosphere, Mars, comet Siding-Spring, Mars Express

27 **Abstract**

28 On 19 October 2014, Mars experienced a very close encounter with Comet C/2013 A1 Siding
29 Spring. Using data from the Mars Advanced Radar for Subsurface and Ionosphere Sounding
30 (MARSIS) on board Mars Express (MEX), we assess the interaction of the Martian ionosphere with
31 the comet's atmosphere and possibly magnetic tail during the orbit of their closest approach. The
32 topside ionospheric electron density profile is evaluated from the peak density of the ionosphere
33 to the local plasma around Mars Express. We find unusual, complex and rapid variability in the
34 ionospheric profile along the MEX orbit, not seen even after the impact of large coronal mass
35 ejections. Before closest approach, large electron density reductions predominate, which could
36 be caused either by comet water-damping, or comet magnetic field interactions. After closest
37 approach, a substantial electron density rise predominates. Moreover, several extra topside
38 layers are visible along the whole orbit at different altitudes, which could be related to different
39 processes as we discuss.

40

41 **Plain Language Summary**

42 The comet Siding-Spring made a single flyby through the Solar System in October 2014, passing
43 very close to Mars on 19 October 2014. For about 10h, the Martian ionosphere (upper
44 atmosphere) was in touch with the cometary atmosphere, also called the coma. In this work, we
45 use data from the Mars Express mission to evaluate the behavior of the ionosphere of Mars at the
46 comet closest approach. We find that the Martian ionosphere suffered a very quick and complex
47 variability with very large density increases and decreases every few kilometers. This variability
48 was caused by the presence of the comet, and we discuss different processes that could have
49 occurred.

50   **1. Context and Motivation**

51   In October 2014, we were witness to an exceptional planetary event in which the atmosphere of

52   a planet was in direct contact with the atmosphere of a comet. This unique event during the space

53   age took place when the Oort-cloud comet named Comet C/2013 A1 (hereinafter Siding Spring)

54   flew by Mars at a distance of only 138,000 kilometers (41.4 Mars radii) during a single flyby

55   through the inner Solar System. Its water production rate at Mars was estimated with in-situ and

56   remote sensing instruments at $1.1\text{-}1.5\pm0.5\times10^{28}$ molecules s^{-1} (Crismani et al., 2015; Schleicher et

57   al., 2014; Bodewits et al., 2015).

58   Several teams have published different aspects of the Martian atmospheric and ionospheric

59   behavior well after Siding Spring's flyby (few hours after), when the cometary dust had been

60   deposited into the Martian atmosphere. In particular, a total dust mass of 82 ± 25 t was deposited

61   in Mars' atmosphere, creating an ionospheric layer of Mg^+ and Fe^+ between 105 and 120 km

62   altitude (Crismani et al., 2018; Benna et al., 2015; Schneider et al., 2015) as measured by the Mars

63   Atmosphere and Volatile Evolution (MAVEN) mission. This layer was also observed by the Mars

64   Advanced Radar for Subsurface and Ionosphere Sounding (MARSIS) on board Mars Express

65   (MEX) (Gurnett et al., 2015; Venkateswara et al., 2016) for two days after the comet encounter.

66   Indeed, this is the largest meteor layer ever observed at a planet other than Earth (Gurnett et al.,

67   2015). In addition, a large total electron content (TEC) increase was recorded by the Mars

68   Reconnaissance Orbiter (MRO) (Restano et al., 2015). The comet also produced large magnetic

69   turbulence in the Martian ionosphere and magnetosheath that lasted several hours after the

70   comet departed (Espley et al., 2015).

71   However, the interaction of the planetary and cometary atmospheres at the time of the closest

72   approach (CA) is largely unknown. One of the main reasons is that all the spacecraft were placed

73   into a protective mode to avoid as much as possible dust impacts from comet sputtering, as dust

74   travelled at the same highly super-sonic speed of the comet, 56 km s^{-1}. For example, the trajectory

75   of MEX was placed such that the spacecraft was mostly protected from the dust by being behind

76   the planet during the comet encounter (from the debris perspective), while MAVEN had most of

77   its payload switched-off having only recently arrived at Mars (the geometry of the encounter is

78   described in the next two sections). In addition, most of the plasma observations during the

79   encounter were very challenging to analyze because 44 h before, a large interplanetary coronal

80   mass ejection (ICME) hit Mars (Witasse et al., 2017), and a large shower of energetic particles into

81   the ionosphere from both the comet and the solar wind was observed at Mars for several days

82   (Sánchez-Cano et al., 2018).

83   Despite these difficulties, there are many data sets still to exploit. The objective of this paper is to

84   examine the MARSIS-MEX dataset at the time of CA before dust had settled in the atmosphere

85   (MEX orbit 13709), and assess the behavior of the Martian ionosphere during its interaction with

86   Siding Spring's coma.

87

2. Geometry of the Encounter

89   Figure 1 shows three different views of the geometry of the encounter at CA, where Siding Spring

90   has been represented as a sphere of radius 15000 km for better visualization (the comet size is

91   only few kilometers). At the time of the encounter with Mars, Siding Spring was moving from the

92   south to the north of the ecliptic plane in a hyperbolic orbit (129° inclination angle) and with a

93   relative speed of ~56 km s^{-1} (JPL Small-Body Database, https://ssd.jpl.nasa.gov/sbdb.cgi?). The

94   CA with Mars occurred at 18:28 UT on 19 October 2014, when the Siding Spring nucleus located

95   relative to the North-Dawn sector of Mars.

96   The comet had a near circular atmosphere (or coma) surrounding the nucleus that can be

97   considered the size of a million kilometers from the comet's nucleus which entirely engulfed Mars

98   for ~10 h (Espley et al., 2015; Sánchez-Cano et al., 2018). The entire MEX orbit 13709 occurred

99   when Mars was inside the coma. In addition, as a typical comet, Siding Spring had two different

100 tails that extend millions of kilometers. The dust tail, which is formed by material from the surface

101 and coma that is blown away due to solar radiation pressure, hit the Martian Southern

102 hemisphere. Figure 2 shows the relative positions of Mars, MEX and Siding Spring at CA. During

103 CA, Mars was partly blocking the dust stream and forming a shadow area for dust impacts in the

104 Northern hemisphere (reddish cylinder in Figure 2b, positions p1 and p2 in Figure 2a), where

105 MEX was placed for security. Therefore, due to their relative position, the Martian southern

106 hemisphere near the morning terminator was the most affected by cometary dust, as this

107 hemisphere was facing toward the cometary particle motion at CA. The peak dust flux was

108 predicted to occur at ~20:06 UT on 19 October (Tricarico et al., 2014) when Mars crossed the

109 comet's orbital plane. In addition to the dust tail, the ion tail also hit Mars for a short period of

110 time. This tail is formed of pickup ions that have joined the flow of the solar wind, adding mass to

111 it and decelerating it, and is surrounded by draped solar wind magnetic field (cometary

112 magnetosphere). Therefore, it is found in opposite direction to the Sun-comet interaction. In

113 principle, Mars was affected by the head of the cometary magnetosphere at CA as we discuss in

114 section 5.

115

116   ### 3. MARSIS Dataset and MEX attitude

117   In this work, we use data from the MARSIS instrument (Picardi et al., 2004; Orosei et al., 2015) on

118   board MEX (Chicarro et al., 2004). MARSIS is a radar that can work in two different operational

119   modes. The first mode is designed to sound the surface and sub-surface of the planet, while the

120   second mode, called Active Ionospheric Sounding (AIS), is designed to sound the topside of the

121   ionosphere of Mars. In this study, we use the MARSIS-AIS dataset that provides electron density

122   profiles of the topside ionosphere (~130-350 km) (e.g. Sánchez-Cano et al., 2012; Morgan et al.,

123   2013). In addition, the AIS dataset also provides information on the spacecraft surroundings

124   (hereinafter referred to as the local plasma) depending on MEX altitude (between ~350 and

125   ~1000 km). Specifically it provides the electron density from the excitation of local electron

126   plasma oscillations, and the magnetic field magnitude from the local cyclotron frequency (e.g.

127   Gurnett et al., 2005; 2008; Akalin et al., 2010; Andrews et al., 2013). The magnetic field measured

128   by MARSIS could originate either from crustal magnetic fields on the Martian surface, or be

129   induced from the solar wind (draped solar wind magnetic field), or both. In this study, we assume

130   that only an induced magnetic field is present in the MARSIS records as MEX was flying above the

131   Northern hemisphere at the time of the MARSIS observations, far from the most intense crustal

132   fields.

133   During an orbit periapsis, MEX typically points toward the planet. However, during the comet

134   encounter, the MEX attitude was different due to operational reasons (the spacecraft was upside

135   down). Fortunately, this issue does not affect MARSIS in AIS mode measurements because the

136   pulses sent out by the instrument propagate roughly spherically in all directions. As a result, the

137   initial reflections always come from the ionosphere via the shortest propagation path which is

138   typically from vertical echoes. Any slant path transmissions will generally not return to the

139   spacecraft, unless the ionosphere is not smooth and there are oblique echoes (e.g., Gurnett et al.,

140   2005; Duru et al., 2006; Andrews et al., 2014).

141

142   ### 4. Observations

143   ### 4.1. Ionosphere between 350 and 1000 km

144   Figure 3 presents the local ionospheric plasma observations at MEX altitude for the orbit of the

145   comet encounter, 13709, as well as for the four previous and three following orbits. For

146   orientation, Figure 3a shows the MEX trajectory during this period. The MEX path through the

147   ionosphere's cavity (below the magnetic pileup boundary) is represented in green, with MEX

148   moving from the North Pole towards the equator, and crossing the day-night terminator from the

149 night to the dayside. Figures 3d-3k show the local electron density and the magnitude of the local

150 magnetic field for consecutive orbits. Since these are observations taken locally at the spacecraft

151 position, they are altitude and solar zenith angle (SZA) dependent. This means that the local

152 electron density should be larger at MEX's pericenter (marked with a P) than at higher altitudes,

153 and also larger for lower SZA (dayside). As mentioned before, the Martian plasma system was

154 affected by an ICME that impacted the planet 44h before the comet encounter. Therefore, in order

155 to help with the analysis, two additional panels have been added showing the local plasma

156 observations for solar wind steady conditions before the ICME hit Mars (Figure 3b), and for the

157 orbit right after the impact of the ICME (Figure 3c). The letters A and B at the top of each panel

158 indicate the start/end of MARSIS detections of electron density above zero, as a proxy for the

159 length of the passage through the ionosphere.

160 For steady solar wind conditions, one expects similar observations to those in Figure 3b as the

161 MEX trajectory does not change very much over the course of a few days. A gradual density

162 increase occurs until pericenter as MEX moves from the night to the dayside and reduces in

163 altitude. It continues to increase after pericenter as MEX is on the dayside and SZA increases. Then

164 there is a plateau for several minutes while MEX ascends and SZA descends until a rapid decrease

165 to lower values occurs, which is typically identified with the transition across the pileup boundary

166 and into the sheath. The magnetic field remains nearly constant at 20 nT for the whole

167 ionospheric transit. However, the scenario is very different after the impact of an ICME. Figure 3c

168 shows a large rise of magnetic field magnitude that remains at 60-80 nT for most of the orbit. It

169 also shows a significant local electron density reduction, with values near 0.5 cm^{-3} at the

170 pericenter, and a sudden increase after periapsis that lasts a minute, where a density of ~3500

171 cm^{-3} is reached. This brief density increase can be associated with the only moment in which MEX

172 transited the proper ionosphere (denser part). The size of the ionosphere passage is largely

173 reduced (see A-B positions) when compared to steady conditions, which means that the

174 ionosphere occurred at lower altitudes than normal. This is due to a large compression of the

175 ionosphere as a result of the ICME passage.

176 Figures 3d-3g show local plasma observations during the recovery of the ICME impact, and just

177 before the Siding Spring flyby (Figure 3h). The magnitude of the magnetic field is reduced from

178 orbit to orbit, while the ionospheric densities gradually become more similar to those in the

179 steady ionosphere (panel b). We note that orbit 13708 (Figure 3g) shows an irregular behavior.

180 The normal transit to the ionosphere occurs between positions A and B, having a sharp density

181 decrease after periapsis that indicates that MEX left the ionosphere (position B). However, there

182 is a moderate increase in density several minutes later when MEX was higher than 700 km,

183 coming back into the ionospheric regime (A*-B*). This is due to a short magnetosheath transit

184   between the positions B and A* most probably caused by a magnetosheath-boundary motion (see

185   e.g. Sánchez-Cano et al., 2017).

186   Figure 3h shows Mars' ionosphere observations at the time of Siding-Spring's CA. These

187   observations are very intriguing as the ionosphere is unusually rarified. MEX density

188   observations at the pericenter are as low as after the passage of the ICME (see Figure 3c for

189   comparisons). However, the size of the MEX ionospheric passage (A-B distance) was standard,

190   and the magnitude of the magnetic field was ~30-40 nT which is close to that for steady

191   conditions and similar to previous orbits. MARSIS-AIS observations indicate that the

192   magnetosheath turbulence found by Espley et al. (2015) during this time did not affect the size of

193   the ionospheric cavity. This means that the magnetic and dynamic pressures exerted by the comet

194   were not enough to move the magnetosheath to lower altitudes as always happens with an ICME.

195   So, in summary, MEX was in the ionosphere from A to B/B*, but between A and 18:27 the electron

196   densities were strongly suppressed. From 18:27 till 18:32, a notable density increase is observed

197   up to ~1500 cm^{-3}, which is not typical for altitudes larger than 700 km in steady conditions. The

198   post-flyby orbit (Figure 3i) also shows a similar level of ionization for similar altitudes, but in this

199   case the cause must be related to the dust deposition within the atmosphere, as corroborated by

200   Benna et al. (2015), who also found several species of metal ions in Mars' atmosphere at similar

201   altitudes with MAVEN observations at the same time as Figure 3i. The sharp density decrease at

202   ~18:32 (letter B) in Figure 3h most probably corresponds to MEX crossing into the

203   magnetosheath region, although our analysis is not conclusive since some ionospheric plasma

204   density is still visible until B*.

205   Figures 3i-3k show the local plasma observations for the orbits after the comet encounter. The

206   post-flyby orbit shows a very robust ionosphere both on the day and nightsides most probably

207   formed by cometary dust deposition. The size of the ionospheric passage is maintained similar to

208   the pre-comet flyby and steady condition orbits, and the level of magnetic field is similar to

209   previous orbits. After that, the ionosphere starts to recover as the density and magnetic field

210   values gradually become normal. The system seems to be recovered by Figure 3k when the

211   longest ionospheric passage of the period is observed.

212   To summarize, the system seems fully recovered from the ICME impact by orbit 13706 (~21 h

213   before CA) in agreement with MAVEN magnetic observations (Espley et al., 2015). During orbit

214   13709, when Mars was inside the outer coma of the comet, there is a notable density decrease up

215   to 18:27 UT (just a minute before CA). At 18:27 UT, local plasma density starts to increase and

216   remains high after CA. The orbit after comet-flyby shows very large local density values for the

217 whole orbit. The system seems to be back to normal conditions by orbit 13712, as seen from
218 MARSIS local plasma parameters.

219

220 **4.2.   Ionosphere between 130 and 350 km**

221 We now focus on the analysis of MARSIS-AIS topside electron density profiles at CA (same orbit
222 as Figure 3h). Similar to the local plasma density, the topside ionosphere also had a very variable
223 behavior. In order to evaluate this electron density variability along the orbit, we use the NeMars
224 model (Sánchez-Cano et al., 2013; 2016a) to compare with the observations. NeMars is an
225 empirical model that describes the electron density distribution with altitude in Mars' ionosphere
226 with respect to SZA, solar activity and heliocentric distance. It is based on Chapman theory
227 adapted to Martian conditions using MARSIS-AIS data. NeMars is ideal for comparisons with these
228 electron density profile observations, as previously demonstrated by other studies such as in
229 support of in-situ Mars crosslink radio-occultations (Ao et al., 2015), solar cycle variations in the
230 Martian ionosphere (Sánchez-Cano et al., 2015b; 2016a; 2016b), annual and solar cycle TEC
231 behavior (Sánchez-Cano et al., 2015a; Cartacci et al., 2018), and ionospheric removal for radar
232 surface studies (Ilyushin et al., 2017).

233 The electron density profile inversions from the ionograms are implemented according to
234 Morgan et al. (2013) and Sanchez-Cano et al., (2012). We note that there is an alternative
235 inversion made by Němec et al. (2017), which is perhaps better for high altitudes (above ~325
236 km) because they used MAVEN observations to fill the gap that MARSIS is not able to sample due
237 to the low power emissions at low frequencies. Instead, Morgan et al. (2013) and Sanchez-Cano
238 et al. (2012) use an empirical shape composed of an exponential dependence. However, NeMars
239 was built based on the Morgan et al. (2013) inversion, and therefore, in order to have consistent
240 comparisons, we prefer to keep the original inversions. Nevertheless, in this study, we do not
241 show data above ~325 km in order to minimize the uncertainty. In addition, we only use data
242 with SZA<85° because the model only works for dayside conditions.

243 Figure 4 shows four MARSIS-AIS topside electron density profiles (blue lines, panels a-d) within
244 less than 8 minutes, and their corresponding NeMars profiles (black dashed lines). These four
245 examples are representative of the overall ionospheric variability observed during orbit 13709.
246 In addition, the corresponding ionograms from which the profiles are retrieved are shown in
247 panels e-h. The first and second profiles (a and b) have a normal behavior from the peak up to
248 200 km (photochemical region). However, they display a significant density decrease above 200
249 km (diffusion region) as compared to the model density profile. On the contrary, the third and

250   fourth profiles (c and d) display a very different ionospheric behavior only a few minutes later. In

251   both cases, the peak altitude is higher than expected, but the density has the same slope as the

252   model up to 200 km (same scale height). However, a significant electron density increase is

253   observed above 200 km, in which several transient ionospheric layers are observed (e.g., at 230

254   and 260 km in panel c and at 250 km in panel d). This is also observed on their respective

255   ionograms (panels g and h), where a cusp structure is clearly seen at ~1.8 MHz. These extra

256   topside layers are a known phenomenon in Mars' upper ionosphere, first reported by Gurnett el

257   al. (2008) and Kopf et al. (2008), but whose explanation is not straightforward. Peter et al. (2014)

258   indicated that changes in the recombination rate (and thus in the electron density) associated

259   with vertical transport and increase in the electron temperature could be the cause. Kopf et al.

260   (2017) recently suggested that these extra layers are related to local current sheets in the upper

261   Martian ionosphere, which could be related to Kelvin-Helmholtz instabilities, magnetic flux ropes,

262   magnetic reconnection, or solar wind magnetic field rotations.

263   Figures 5a and 5b present all electron density profiles that could be retrieved from the orbit of

264   the CA (13709), as well as the expected altitude of the main ionospheric peak (gray dashed-line)

265   from the model. To perform a sensible comparison avoiding the normal variability associated

266   with SZA, the relative electron density differences between the AIS observations and the

267   corresponding NeMars value for each data condition are color-coded. Reddish colors indicate an

268   excess of density with respect to the model while blueish colors indicate a reduction. In particular,

269   NeMars was run as normal in Figure 5a, while in Figure 5b the model was fixed by the observed

270   peak electron density. Both panels show the variability of this set of profiles but focusing on

271   different aspects: Figure 5a emphasizes density changes at all altitudes, and Figure 5b highlights

272   scale height changes. To support the observations, the peak electron density, topside TEC, local

273   plasma density from Figure 3h, as well as the MEX altitude, latitude and SZA are shown in Figures

274   5c-5f, respectively.

275   In general, the topside ionosphere is found to be much less dense than expected. In the

276   photochemical region (below ~200 km), most of the profiles do not show a large variation with

277   respect to the expected densities (shades of white in Figure 5a), with few exceptions at ~18:21,

278   ~18:23, ~18:26 and ~18:30 UT. Also, they do not show a large variation in scale height (shades

279   of white in Figure 5b) with the exception of a large reduction between ~18:21 and ~18:22 UT

280   and ~18:23 and ~18:26 UT. The largest variations occur within the diffusion region above ~200

281   km. Large density reductions (up to 40% in some cases) are observed from ~18:19 till 18:24 UT

282   and from 18:25 till 18:27 UT in Figure 5a. They occur at low northern latitudes, on the dayside,

283   and at the same time as the local plasma density (Figure 5e) and TEC reductions (Figure 5d). This

284   suggests that the complete dayside ionospheric structure above the photochemical region
285   sampled by MEX was affected by the comet.

286   However, in the course of a few minutes, the ionosphere also showed notable density increases.
287   The most moderate increase occurred between ∼18:18 and 18:19 UT coinciding with a significant
288   local density rise (Figure 5a). During this time, the largest density variations occurred at ∼210-
289   250 km, which indicates that transient layers similar to Figure 4c were present. There was
290   another moderate increase above ∼210 km between ∼18:24 and 18:25 UT although the local
291   plasma density remained very low and the scale height (Figure 5b) was smaller than the model.
292   This means that these profiles had a shape similar to that of the first and second profile in Figure
293   4 but lifted to higher altitudes. The largest density variations occurred from ∼18:27 UT onwards
294   when MEX was above 500 km flying at low northern latitudes and lower SZA, coinciding with an
295   increase in local plasma density (Figure 5e). During this period (∼18:27 UT onwards), the
296   ionospheric density was raised by at least 40% in most of the profiles. These increases were
297   mostly observed at ∼230-260 km altitude, indicating the presence of several transient layers as
298   in Figure 4.

299   Another important aspect to consider is the ionospheric peak density variability. In general, this
300   parameter is very stable along an orbit having values typically very close to those predicted.
301   Figure 6 compares the peak electron density of the CA orbit (13709, circles in blue) and the orbit
302   before the comet encounter (13708, stars in yellow). During the CA orbit, an unusual large
303   variability is observed along the whole orbit with significant density rises that contrast with the
304   relatively smooth behavior of the pre-comet flyby orbit. This variability is most likely caused by
305   the comet interaction with the Martian atmosphere and solar wind, and not by the transit of the
306   ICME because the system seems totally recovered in previous orbits as shown by several
307   parameters, i.e. normal ionospheric peak behavior (Figure 6 yellow stars), recovered local plasma
308   observations (Figure 3g), and also normal magnetospheric conditions (Espley et al., 2015).

309

310   5. Discussion: What Caused the Large and Sudden Martian Ionospheric Variability?

311   In the course of a few minutes, the ionosphere of Mars showed very unusual and variable
312   behavior with large density increases and reductions that seem not to be related to the typical
313   variability sources, i.e. changes in solar flux or neutral atmospheric conditions. In this section, we
314   discuss possible drivers of this variability.

315

316   **5.1.   Density increase after 18:27 UT**

317   Particles in the coma and dust tail followed the trajectory of the comet at highly super-sonic
318   speeds, moving altogether at the speed of the comet 56 km s^{-1}. Since at CA Mars was completely
319   engulfed by the comet's coma, the whole planet was affected by different cometary particles (e.g.
320   Crismani et al., 2015; 2018; Gurnett et al., 2015; Sánchez-Cano et al., 2018). However, the
321   southern dawn hemisphere was in fact much more affected because it faced towards the
322   cometary dust particle motion. Figure 2a shows four Mars-MEX instants as seen from Siding
323   Spring field-of-view, and Figure 2b shows the relative position of Mars, MEX and Siding Spring
324   from the comet velocity reference frame. In order to protect the spacecraft and their instruments
325   from particle debris impacts, MEX was located above the northern hemisphere and dusk sector
326   during the CA (shadow cylinder area in Figure 2b). This mean that although still affected by the
327   coma, it was in the least risky place with respect to debris impacts because Mars itself acted as a
328   shield for those particles. However, the shielding only lasted for part of the orbit, resulting in
329   MEX encountering the debris stream from 18:25 UT (see MEX position outside the shadow
330   cylinder in Figure 2b, and positions p3-p4 in Figure 2a), and coinciding with the density
331   enhancements in both local plasma and density profiles.

332   As described before, most of the density enhancements come from extra layers in the topside
333   ionospheric profiles, which could be caused by plasma instabilities, dust ablation, or different
334   energy pick-up ions. We note that these transient layers are identified and retrieved from the
335   ionograms where the ionospheric trace exhibits a cusp structure (see an example in Figure 4g-h).
336   This type of structure corresponds to a nonmonotonic form, for which standard inversion
337   schemes are not set up. Therefore, the electron density profile inversion obtained here is just an
338   indication of a change in those regions and may not be entirely precise. In addition, the
339   uncertainty at high altitudes can propagate to lower altitudes, biasing the peak altitude to too
340   larger values.

341   Plasma instabilities caused by the relative velocity between the Martian ionosphere and the
342   cometary coma could be the cause for these extra topside layers as in e.g. Kopf et al. (2017).
343   Unfortunately, we do not have enough observations to analyze this scenario. Other potential
344   factors that could have helped in the formation of a denser ionospheric region are MEX travelling
345   within lower SZAs and more equatorial latitudes (i.e. near the area most affected by dust
346   particles), or that Mars was in the densest possible part of the transited coma at this time (i.e.,
347   CA). In addition, as said before, we note that the existence of an overhang in the ionospheric trace
348   (e.g. Figure 4g-h) might lead to underestimating the altitude of the ionospheric peak in the
349   electron density profile.

350   Dust ablation in the atmosphere could be a cause for this density increase. Dust ablation is

351   expected to settle below the main ionospheric peak (~90-100 km), but can also have an effect at

352   higher altitudes when precipitating. However, Crismani et al. (2018) found in a comprehensive

353   analysis that the meteor shower lasted less than 3 h, was limited to one hemisphere, and that

354   horizontal winds globally redistributed this material over the next two days. Benna et al. (2015)

355   also found that ~20h after the flyby, several metallic ions were present at 185 km altitude, which

356   could have been transported by eddy and ambipolar ion diffusion from ~115 km up to 185 km.

357   This phenomenon can explain the large local density values observed during the post-flyby orbit

358   (Figure 3i). However, we do not think the extra topside layers during CA could have been formed

359   almost immediately by this process, since MEX was not in the most affected region (Figure 2b).

360   At CA the atmosphere will have only been in reasonably dense coma for a few tens of minutes,

361   which gives not enough time for redistribution.

362   Pickup ions from the solar wind could be another feasible scenario. Sánchez-Cano et al. (2018)

363   indicated that for the ~10h period that Mars was at less than a million kilometer distance from

364   the comet, a significant amount of oxygen pickup ions entered Mars' atmosphere, with the pickup

365   ion flux maximizing at CA. The simulation performed by Sánchez-Cano et al. (2018) indicates that

366   O^+ particles with energies of 1 keV were deposited in Mars' atmosphere between 140 and 160

367   km, having a secondary energy loss peak at ~170 km. However, the energy loss associated with

368   O^+ pickup ions with energies of 1 keV and lower may not be enough to produce a significant

369   electron density increase in Mars' ionosphere (e.g. Wang et al., 2016), as well as one should expect

370   that generally, O^+ pickup ions will be higher energy. In addition, higher energetic O^+ pickup ions

371   were predicted to be deposited lower in the ionosphere. These particles are an important source

372   of atmospheric heating and ionization when they precipitate and lose their energy in Mars'

373   atmosphere. Although difficult to observe with the limited instrumentation that was in operation

374   during CA, the extra density observed at the ionospheric peak (reddish colors) in several profiles

375   of Figure 5a could be related to those energetic pickup ions.

376   We conclude that MEX encountering the debris stream as well as pick-up ions seem plausible

377   scenarios for explaining these large electron density increases after 18:27 UT, near the time of

378   CA. Unfortunately, the lack of observations at CA does not allow us to get a firm conclusion. More

379   detailed ionospheric modelling of dust and pick-up ion deposition is needed to get more insights

380   on how Mars' ionosphere behaved.

381

382

383   **5.2.   Density decrease before 18:27 UT**

384   The large density reduction observed at high altitudes during the start of the orbit until 18:27 UT

385   occurred when MEX was shielded by Mars from the cometary debris stream (Figure 2), but still

386   affected by the coma. For those illumination conditions, as well as spacecraft altitude and

387   planetographic conditions, electron density observations should be similar to the NeMars

388   predictions as for the previous orbit. A possible reason is that the coma shielded Mars'

389   atmosphere from some solar extreme-ultraviolet (EUV) wavelengths. Since MARSIS detected the

390   ionospheric peak at a typical density level, only the less energetic EUV fluxes would be affected,

391   and therefore, less ionization would occur at high altitude. However, this hypothesis is unlikely

392   to be the reason because previous studies have found that comets with a similar production rate

393   and closer to the Sun (at 1 AU), do not attenuate the solar EUV flux even at close distances to the

394   nucleus (Bhardwaj, 2003; Vigren and Galand, 2013). This effect is expected to be even smaller for

395   Mars' distance.

396   Induced magnetic fields from the solar wind can produce density reductions in the topside

397   ionosphere (e.g. Russell and Vaisberg, 1983). During CA, a magnetic field of ~30-40 nT was

398   present at MEX altitude that could be enough to compress the topside profile (e.g. Morel et al.,

399   2004; Sánchez-Cano et al., 2015b; Ramírez-Nicolás et al., 2016). If we assume that the magnetic

400   field is only from the solar wind, this hypothesis seems unlikely because the field is of the same

401   level as previous orbits and only slightly larger than for steady conditions. If this field was

402   responsible, all topside profiles from previous orbits should show a similar behavior, which is not

403   the case. However, we have to consider that the local magnetic observations for orbit 13709 are

404   a mix of solar wind and cometary magnetic fields, which in turn are a distorted version of the

405   draped solar wind magnetic field. Espley et al. (2015) indicate that at CA, a strong rotation of the

406   in-situ magnetic field was observed by MAVEN as the comet approached, draping the cometary

407   magnetic field over Mars. Although we do not have an estimation of the radius of the comet

408   magnetic tail, it can be assumed that the magnetic rotation observed by Espley et al. (2015) is a

409   consequence of the comet magnetic tail interaction with Mars, as Mars was at $\sim 10^5$ km of the

410   nucleus during CA. The ionospheric magnetic field observed by MAVEN experienced several

411   small-scale magnetic field structures with excursions up to 45 nT (Espley et al., 2015), which

412   confirms MARSIS observations of local magnetic field variability (Figure 3h). Consequently, these

413   small-scale magnetic distortions caused most probably by the comet magnetic tail interaction

414   could be a reasonable cause for the somewhat disordered ionospheric reductions observed by

415   MARSIS. Unfortunately, MEX does not have a proper magnetometer for in-situ comparisons.

416   Other possible reasons are cometary dust and gas interaction with the Martian atmosphere as
417   they are the main component of the coma. Focusing on the dust first, electrons within the
418   ionosphere can be lost due to dust attachment. This is well-known at low and mid altitudes in the
419   Martian atmosphere, especially on the nightside where aerosols tend to negatively charge due to
420   electron attachment when the level of suspended Martian dust is high (Cardnell et al., 2016).
421   Preliminary results from the Planetary Fourier Spectrometer (PFS) (Formisano et al., 2005) on
422   board Mars Express indicate an increase of dust in the Martian atmosphere after the comet's
423   closest approach, especially in the latitude range 40°S-10°N (Giuranna et al., 2017). However,
424   MAVEN observed that ~82 t were deposited in Mars' atmosphere over ~3h and limited to the
425   Martian hemisphere facing the comet (the opposite hemisphere to where MEX was) (Crismani et
426   al., 2018). Although dust within the coma could still have interacted with the ionosphere which
427   was transited by MEX, and have some localized effects, it seems unlikely to be the main cause of
428   the ionospheric reduction.

429   Water is the other main component of the coma, such that electron dissociative recombination
430   caused by water molecules could be another plausible cause for the observed reduction in
431   electron density. Yelle et al. (2014) predicted that cometary water molecules would penetrate
432   into the Martian atmosphere to an altitude of ~150 km and would most likely be the major source
433   of variability from the coma at high altitude. The influx of cometary water would produce a
434   significant hydrogen increase as a consequence of multiple chemical reactions that eventually
435   reduce the density of ionospheric electrons at those altitudes and above (see reactions R8, R9,
436   R12 and R16 of Yelle et al., 2014). The same phenomenon, but with different chemistry, has been
437   observed at Earth during rocket launches, which introduce a large abundance of H_2O, H_2 and CO_2
438   molecules into the upper ionosphere, resulting in sudden electron density reductions (e.g.
439   Mendillo et al., 1975; 1981). These electron density reductions are very fast, lasting as long as the
440   water source is present. A similar process has also been observed at Saturn, where water-based
441   showers from the rings reduce the electron density of the equatorial Saturnian ionosphere
442   (O'Donoghue et al., 2013; Moore et al., 2015). Moreover, the impact of comet P/Shoemaker–Levy
443   9 with Jupiter in 1994 also produced a localized significantly reduction of the ionospheric H_3^+
444   emissions (e.g. Kim et al., 1996), which modelling confirmed to coincide with electron density
445   reductions on the same areas right after the impact. Modeling suggests that cometary water was
446   the cause for both electrons and H_3^+ reductions (Maurellis and Cravens, 2001). Based on MAVEN
447   observations, Crismani et al. (2015) determined that Siding Spring deposited a total mass of 24 t
448   of water gas in Mars' atmosphere, and that cometary hydrogen delivered to the planet from water
449   and its products was $3.4\pm1.7\times10^{12}$ atoms/cm², which is comparable with but smaller than the
450   Martian hydrogen abundance above 150 km. Although a global perturbation seems implausible

451 in terms of the total mass deposited into the whole Mars' atmosphere, the coma is very rich in
452 water species that expands for at least a million kilometers surrounding the comet and could have
453 had a notable damping effect in Mars' atmosphere during the ~5 h that Mars was immersed in
454 the coma. Therefore, in the region not directly affected by comet sputtering (shadow cylinder in
455 Figure 2b), it is reasonable to consider that some localized effects could occur similar to those fast
456 reductions observed at the rocket's launches at Earth which in turn would explain the high
457 variability observed in Mars' ionosphere.

458 Therefore, we conclude that either cometary magnetic field or water-damping seem plausible
459 scenarios for explaining these large electron density decreases before 18:27 UT, although water
460 seems the more favorable scenario based on previous cometary encounters, such as comet
461 P/Shoemaker–Levy 9. The lack of observations does not allow us to get a firm conclusion, but
462 more detailed ionospheric modelling could be a reasonable next step to understand this behavior.

463

464   **6. Conclusions**

465 We assess the interaction of the Martian ionosphere with comet Siding Spring's coma and
466 magnetic tail during the orbit of their closest approach, when both atmospheres where in direct
467 interaction. The study employs Mars Express MARSIS observations from orbit 13709 on 19
468 October 2014 at ~18:30 UT, closest approach compared with surrounding orbits. During this
469 time, the ionosphere of Mars showed very unusual behavior, having an extreme variability not
470 seen even after the impact of large ICMEs.

471 The ionospheric behavior is evaluated through local plasma observations (electron density and
472 magnetic field intensity local to the spacecraft), as well as though electron density profiles of the
473 ionosphere determined by topside sounding (~130-350 km). We find a very complex and rapid
474 variability along the Mars Express orbit at all altitudes, not typical of this area and solar
475 illumination conditions, which is also not related to space weather activity. Before closest
476 approach, large density reductions predominate above 150 km while after closest approach, a
477 substantial density rise prevails at all altitudes. Moreover, several extra topside layers are visible
478 along the whole orbit at different altitudes. We have discussed different causes for this elevated
479 ionospheric variability, especially the large density reduction, which seems more plausible to be
480 caused by comet water-damping.

481 The single flyby of comet Siding-Spring to Mars produced massive effects on its ionosphere on a
482 global scale. Therefore, understanding the interaction of the atmosphere/ionosphere of both

483   bodies is very important in order to assess early Mars, as well as the evolution of terrestrial planet

484   atmospheres from times in which comet flybys and impacts occurred more often than now.
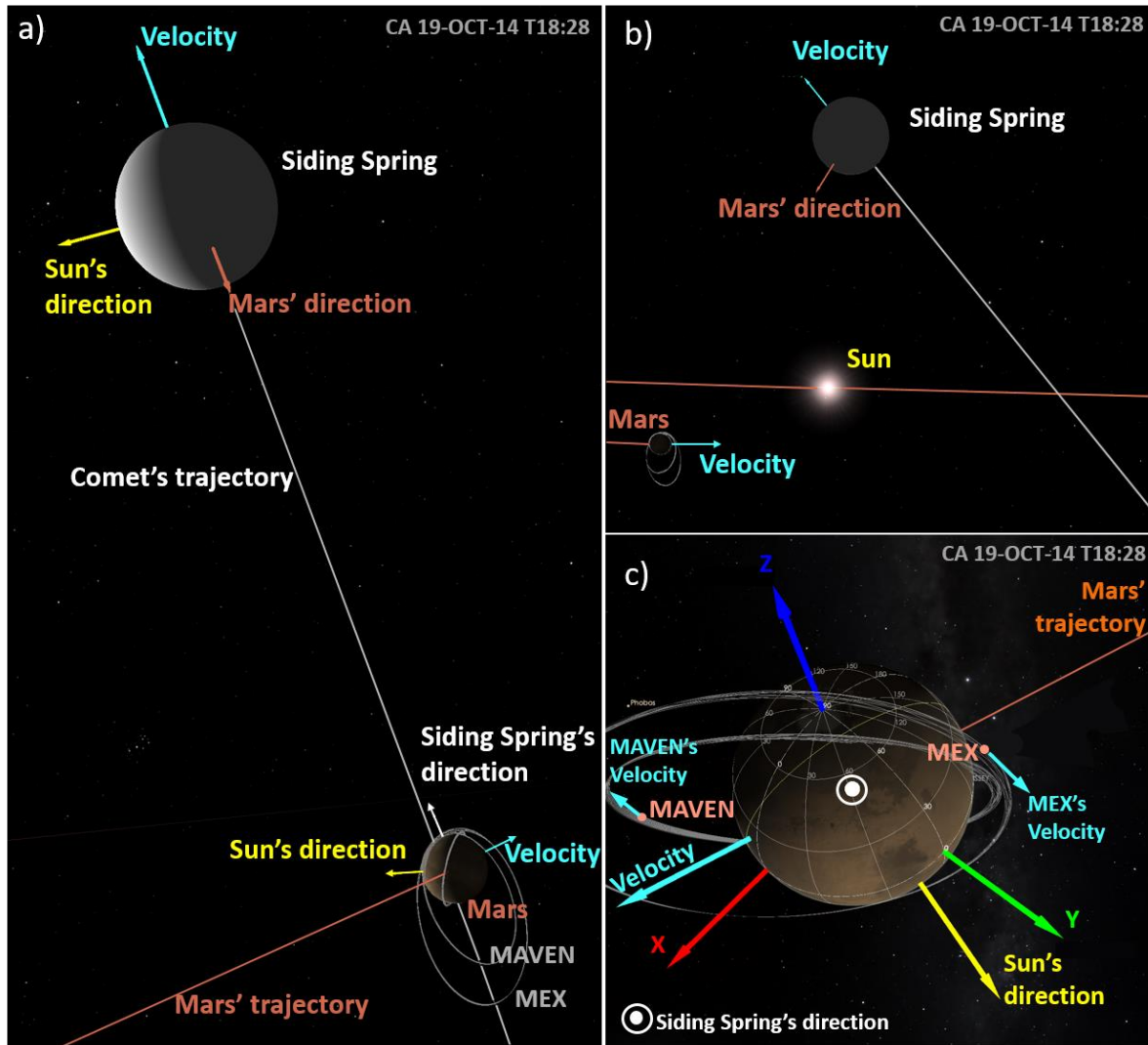
485

Acknowledgments

491

492

493

Figure 1: Mars-comet encounter at CA. Siding-Spring had a hyperbolic orbit with an inclination angle of 129° and moved from south to north of the ecliptic at the time of CA, traveling at a relative speed of ~56 km/s. At CA, the comet head relative position with respect to Mars was toward the North and Dawn Martian hemispheres. However, the comet tail that follows the comet was still moving from the south to the north of the ecliptic. Therefore, the southern and dawn Martian hemispheres were the most affected by dust. For better visualization, comet Siding-Spring has been represented as a sphere of radius 15000 km. Panels (a) and (b) are adapted from Sánchez-Cano et al. (2018). (a) Side view of Mars and the comet. (b) View of the Sun, Mars and the comet from behind Mars. (c) Mars as seen from the comet. X, Y and Z are the vector coordinates of Mars in a body fixed frame.
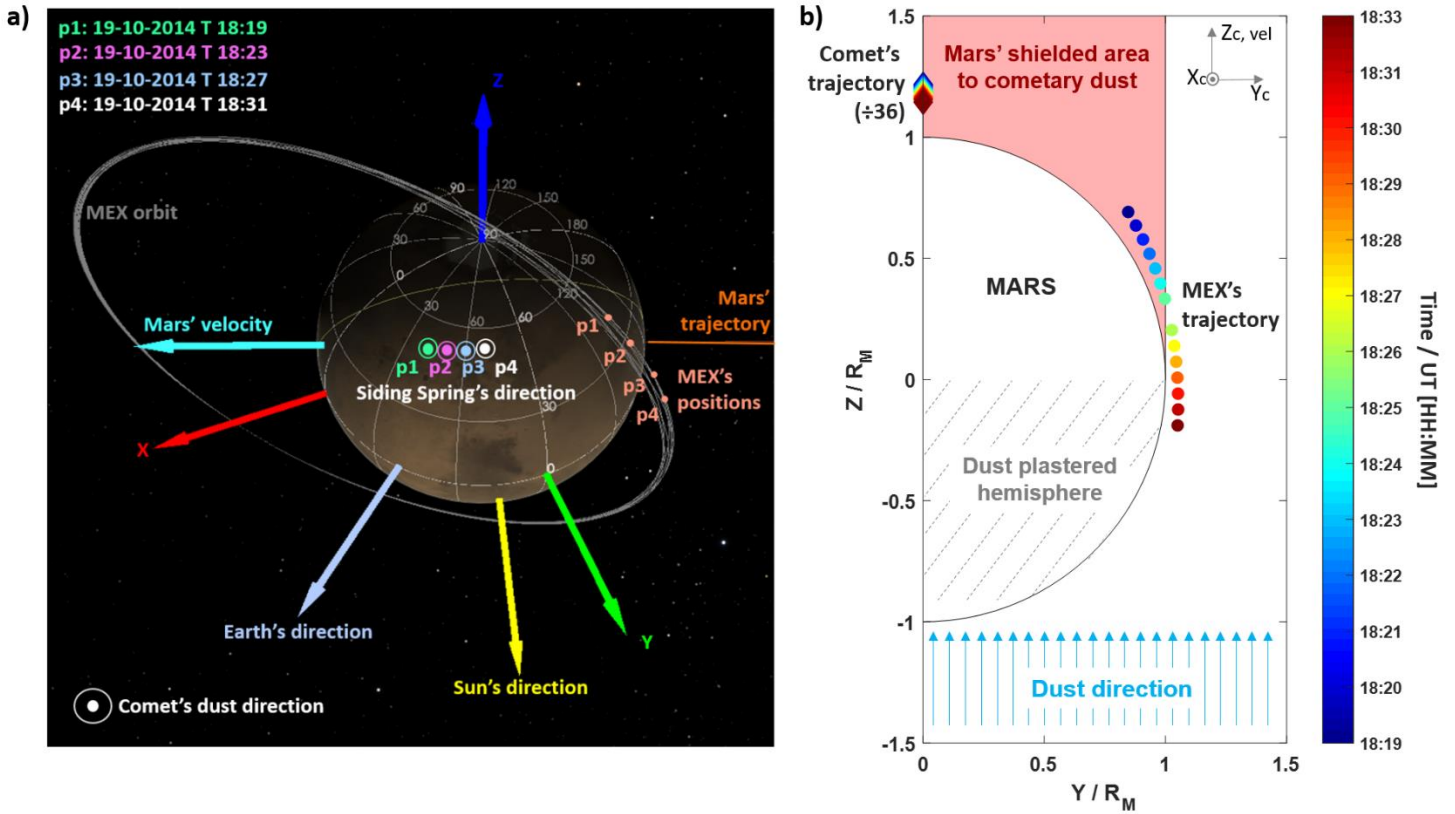
507 **Figure 2:** Geometry of the Mars-comet-MEX encounter within an interval of 14 min. (a) Mars and
508 MEX as seen from the comet at 18:19 UT (green), 18:23 UT (pink), 18:27 UT (light blue), and
509 18:31 UT (white). X, Y, and Z are the vector coordinates of Mars in a body fixed frame. In this
510 figure, the comet's head is northward with respect to Mars (where the readers are). (b) Mars,
511 comet and MEX in the comet velocity frame (Mars's rest frame), where the Z_c direction follows
512 the relative velocity vector of the comet with respect to Mars, and X_c points to the Sun. The comet
513 position has been divided by 36 Martian radii for better visualization. While the comet is at the
514 north of Mars (diamonds), the dust tail is still following the comet's head, hitting Mars from the
515 south, specially the southern hemisphere (dust plastered hemisphere). Mars is partly blocking
516 the dust stream and forming a shadow area for dust impacts in the northern hemisphere (reddish
517 cylinder). This shadow cylinder is formed in the direction of their relative velocity vector.
518 Therefore, Mars is shielding MEX up to ~18:25 UT (p1 and p2 in (a)), but not later. In addition to
519 this, we note that the comet's coma is engulfing the whole planet in this figure as its radius is
520 about a million kilometers from the head of the comet.
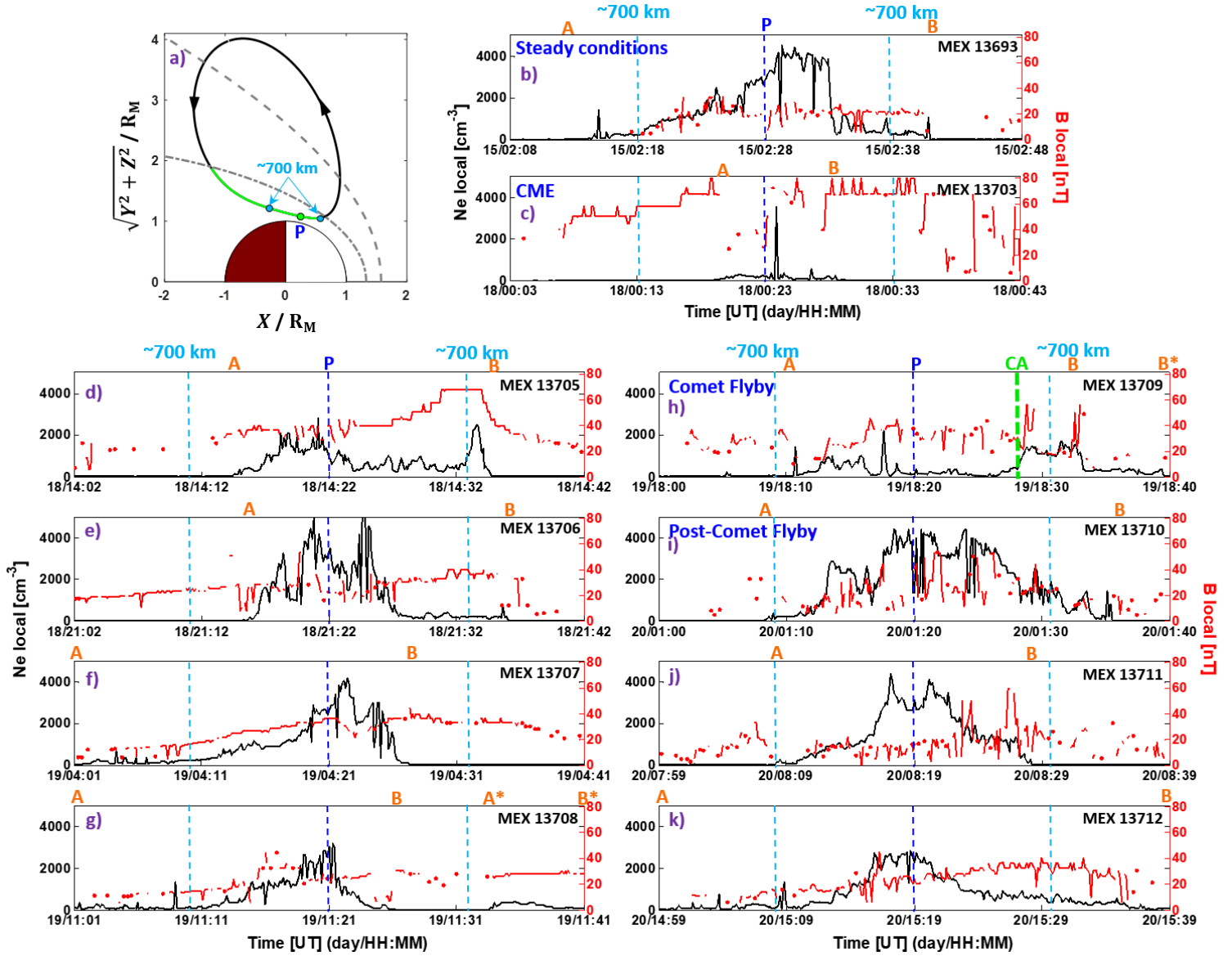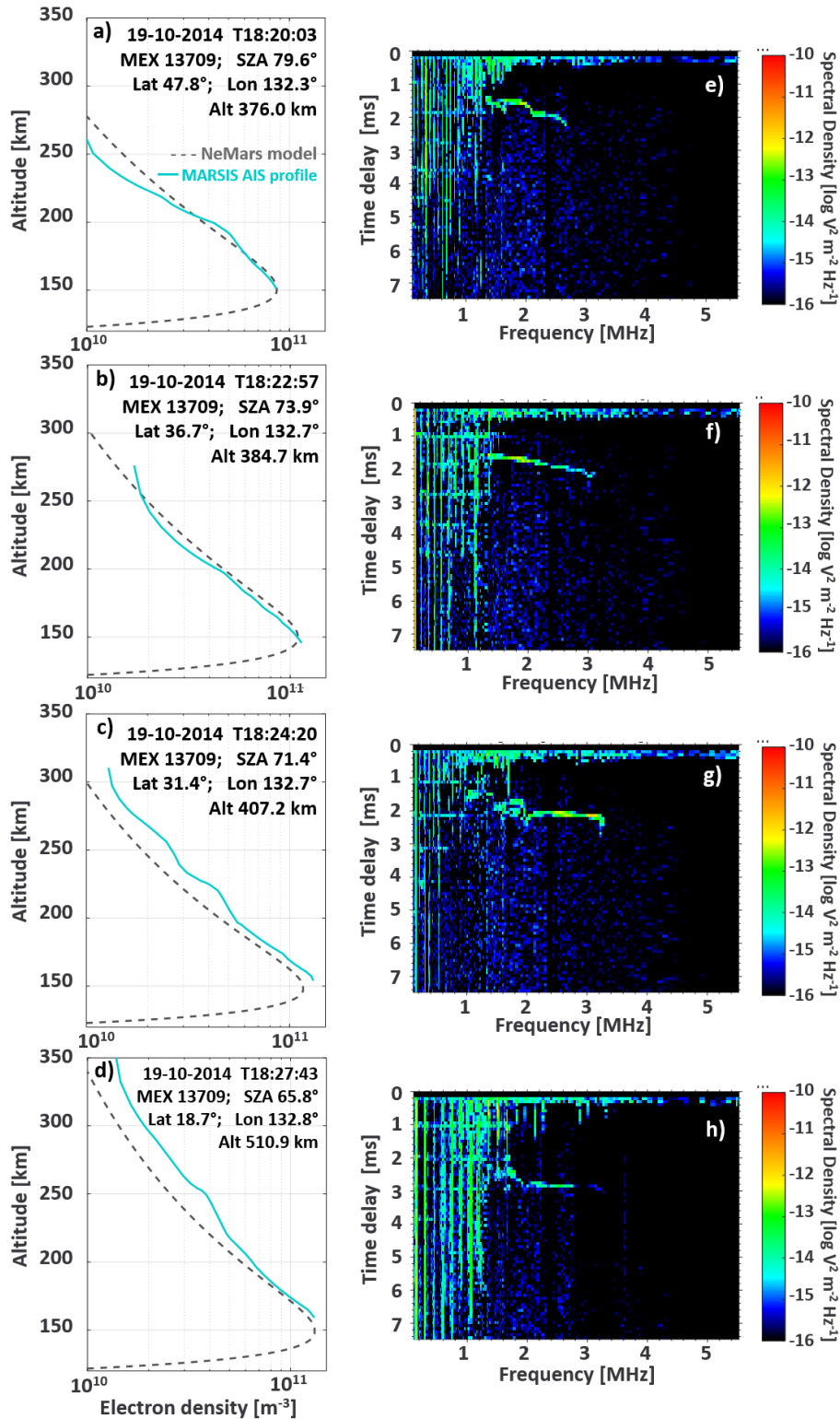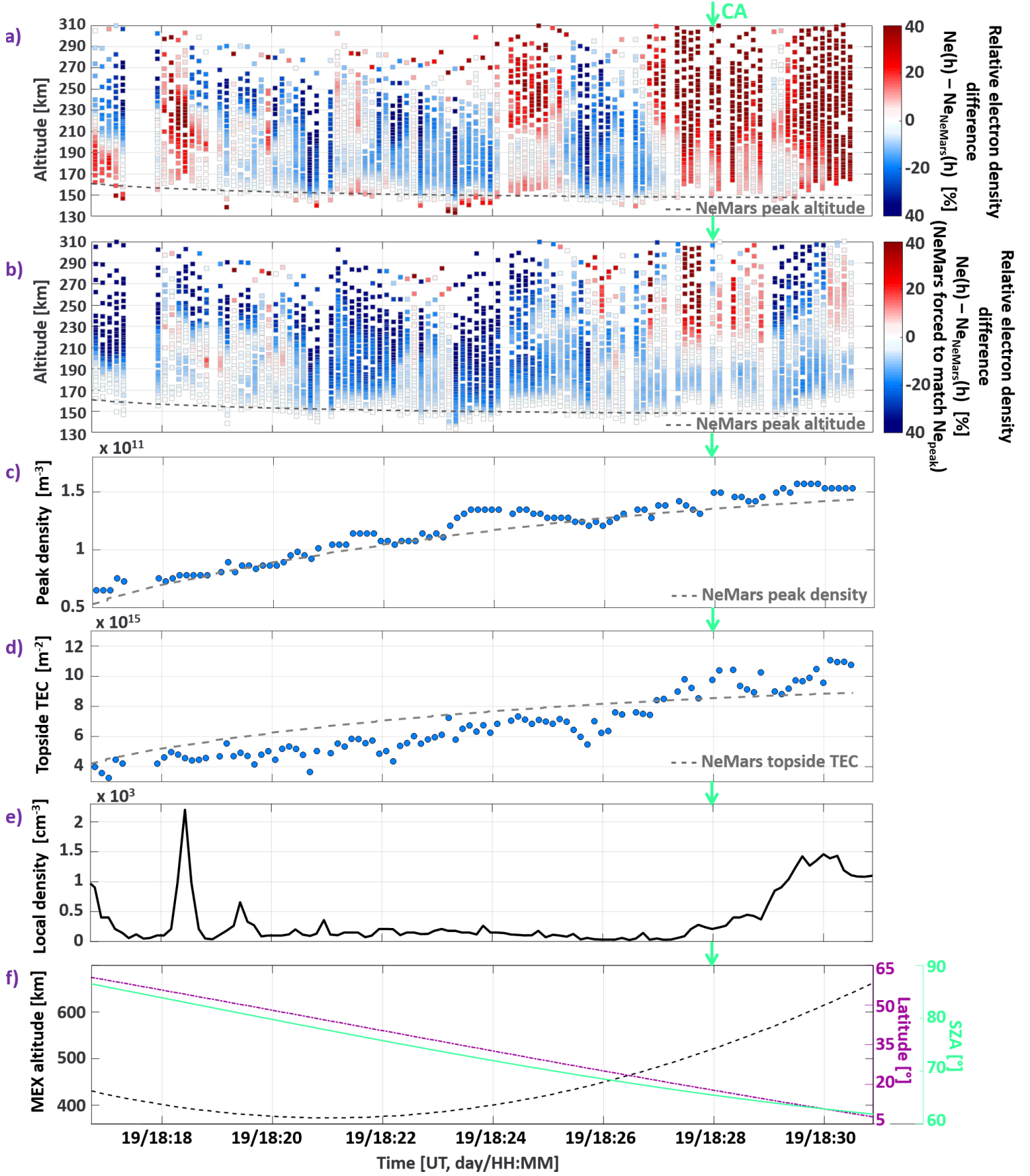
521

Figure 3: (a) Mars Express trajectory in MSO-cylindrical coordinates (in black), and its transit within the ionosphere cavity (in green). The Sun is to the right. A grey dashed-dotted line indicates the magnetic pileup boundary position (Edberg et al. 2008), and a grey dashed line the bow shock position (Hall et al. 2016). The pericenter is marked with a P and a green dot. The 700 km altitude points are marked with blue dots. (b-k) MARSIS local plasma observations of the ionosphere of Mars at MEX altitude. Each panel shows local electron density (in black) and local magnetic field (in red) from a different orbit. In each panel, the periapsis is indicated with a P and a dark-blue dashed-line, and the times when the orbit was at 700 km are marked with a light-blue dashed-line. A and B correspond to the times at which the local plasma density starts/ends being different from zero. In panel (h), the time of comet CA is also indicated with a green dashed-line. Orbit examples for steady conditions and for the impact of a CME are shown in (b) and (c) respectively.

535

536

537 **Figure 4:** (a-d) Four representative MARSIS-AIS electron density profiles (cyan) from orbit
538 13709 and the corresponding NeMars profile for reference (gray dashed-line). (e-h) Ionograms
539 from which the electron density profiles in (a-d) were retrieved.

540

541   **Figure 5:** Ionospheric parameters for MEX orbit 13709 for SZA<85° and altitude lower than 700

542   km (where more accurate electron density profiles can be retrieved). (a) Altitude electron density

543   profiles plotted versus time along the MEX orbit. Electron density values are color-coded

544   according to the percentage of density relative variation of the MARSIS-AIS observations with

545   respect to the NeMars model. Reddish colors mean an excess of electron density and blueish

546   colors a density deficit. The NeMars peak altitude is plotted as a gray dashed-line for reference.

547   Discontinuities in each vertical column are caused by different data sampling, as not always it is

548   possible to obtain uniformly spaced data from the ionogram trace. (b) Same than (a) but where

549   NeMars values are forced to fit the AIS peak density. (c) Peak density from AIS profiles. The

550   NeMars peak density is plotted as a gray dashed-line for reference. (d) Topside TEC from AIS

551   profiles. The NeMars topside TEC is plotted as a gray dashed-line for reference. (e) Local plasma

552   density along the orbit (same as Figure 3h). (f) Mars Express altitude (black), latitude (purple)

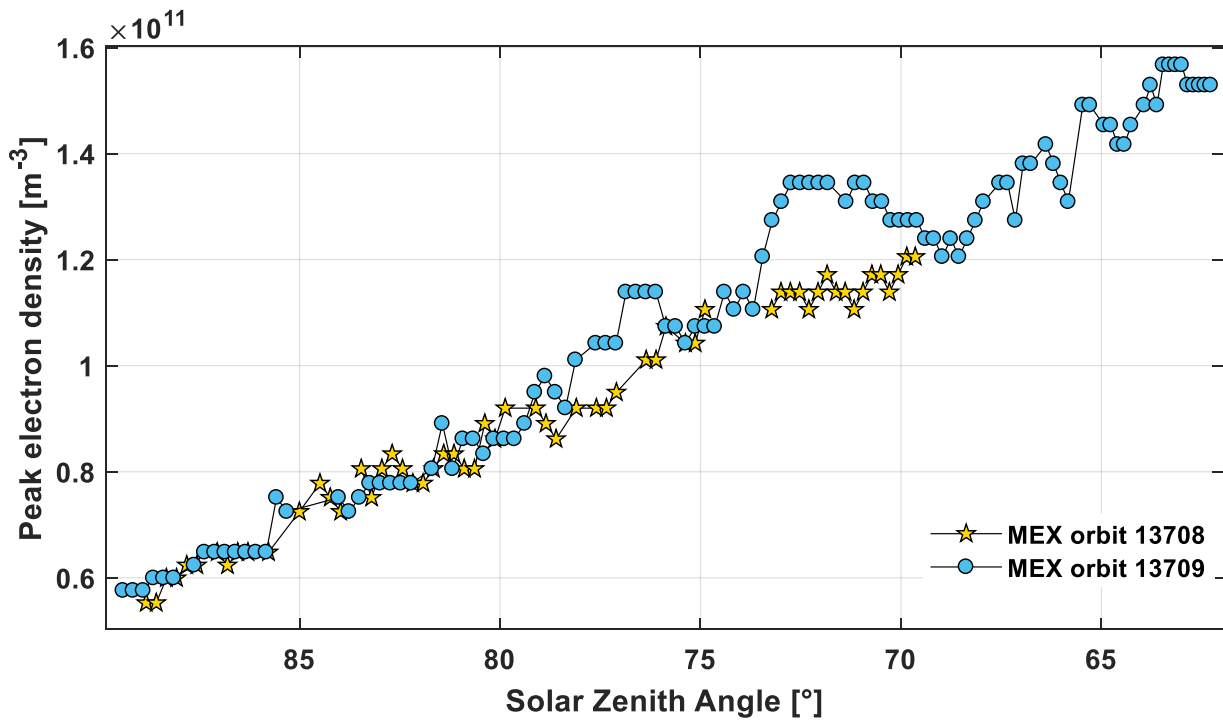553   and solar zenith angle (SZA, green).

554

555

556

557   **Figure 6:** Peak density from AIS profiles from the MEX orbit before the comet encounter (yellow

558   stars) and the orbit of the encounter (blue circles).

559

560 **References:**

561 — Akalin, F., D.D. Morgan, D.A. Gurnett, D.L. Kirchner, D.A. Brain, R. Modolo, M.H. Acuña, J.R.
562   Espley, (2010), Dayside induced magnetic field in the ionosphere of Mars, *Icarus*, 206, 104–
563   111, doi:10.1016/j.icarus.2009.03.021

564

565 — Andersson, L., et al. (2015), Dust observations at orbital altitudes surrounding
566   Mars, *Science*, 350, 6261, doi:10.1126/science.aad0398.

567

568 — Andrews, D. J., H. J. Opgenoorth, N. J. T. Edberg, M. Andre, M. Franz, E. Dubinin, F. Duru, D.
569   Morgan, and O. Witasse (2013), Determination of local plasma densities with the MARSIS
570   radar: Asymmetries in the high-altitude Martian ionosphere, J. Geophys. Res. Space Physics,
571   118, 6228–6242, doi:10.1002/jgra.50593.

572

573 — Andrews, D. J., M. André, H. J. Opgenoorth, N. J. T. Edberg, C. Diéval, F. Duru, D. A. Gurnett, D.
574   Morgan, and O. Witasse (2014), Oblique reflections in the Mars Express MARSIS data set:
575   Stable density structures in the Martian ionosphere, J. Geophys. Res. Space Physics, 119, 3944–
576   3960, doi:10.1002/2013JA019697.

577

578 — Ao, C. O., C. D. Edwards Jr., D. S. Kahan, X. Pi, S. W. Asmar, and A. J. Mannucci (2015), A first
579   demonstration of Mars crosslink occultation measurements, Radio Sci., 50,
580   doi:10.1002/2015RS005750.

581

582 — Benna, M., Mahaffy, P. R., Grebowsky, J. M., Plane, J. M. C., Yelle, R. V., and Jakosky, B.M. (2015).
583   Metallic ions in the upper atmosphere of Mars from the passage of comet C/2013 A1 (Siding
584   Spring). Geophys. Res. Lett., 42, 4670–4675, doi:10.1002/2015GL064159.

585

586 — Bhardwaj, A., On the Solar EUV Deposition in the Inner Comae of Comets with Large Gas
587   Production Rates, Geophys. Res. Lett., 30(24), 2244, doi:10.1029/2003GL018495, 2003.

588

589 — Bodewits, D., Kelley, M. S. P., Li, J., Farnham, T. L., & A'Hearn, M. F. (2015). The pre-perihelion
590   activity of dynamically new comet C/2013 A1 (Siding Spring) and its close encounter with
591   Mars. The Astrophysical Journal Letters, 802(1), L6. https://doi.org/10.1088/2041-
592   8205/802/1/L6

593

594 − Cardnell, S., O. Witasse, G. J. Molina-Cuberos, M. Michael, S. N. Tripathi, G. Déprez, F.
595   Montmessin, and K. O'Brien (2016), A photochemical model of the dust-loaded ionosphere of
596   Mars, J. Geophys. Res. Planets, 121, 2335–2348, doi:10.1002/2016JE005077.
597

598 − Cartacci, M., Sánchez-Cano, B., Orosei, R., Noschese, R., Cicchetti, A., Witasse, O., et al. (2018).
599   Improved estimation of Mars ionosphere total electron content. Icarus, 299, 396–410.
600   https://doi.org/10.1016/j.icarus.2017
601

602 − Chicarro, A., Martin, P., & Trautner, R. (2004). The Mars Express mission: An overview. In A.
603   Wilson & A. Chicarro (Eds.), Mars Express: The scientific payload (Vol. 1240, pp. 3–13).
604   Noordwijk, Netherlands: ESA Special Publication
605

606 − Crismani, M. M. J., et al. (2015). Ultraviolet observations of the hydrogen coma of comet C/2013
607   A1 (Siding Spring) by MAVEN/IUVS. Geophys. Res. Lett., 42, doi:10.1002/2015GL065290.
608

609 − Crismani, M. M. J., Schneider, N. M., Evans, J. S., Plane, J. M. C., Carrillo-Sánchez, J. D., Jain, S., et
610   al. (2018). The impact of comet Siding Spring's meteors on the Martian atmosphere and
611   ionosphere.   Journal   of   Geophysical   Research: Planets,   123.
612   https://doi.org/10.1029/2018JE005750
613

614 − Duru, F., D. A. Gurnett, T. F. Averkamp, D. L. Kirchner, R. L. Huff, A. M. Persoon, J. J. Plaut, and G.
615   Picardi (2006), Magnetically controlled structures in the ionosphere of Mars, J. Geophys. Res.,
616   111, A12204, doi:10.1029/2006JA011975.
617

618 − Edberg, N. J. T., M. Lester, S. W. H. Cowley, and A. I. Eriksson (2008), Statistical analysis of the
619   location of the Martian magnetic pileup boundary and bow shock and the influence of crustal
620   magnetic fields, J. Geophys. Res., 113, A08206, doi:10.1029/2008JA013096.
621

622 − Espley, J. R., et al. (2015). A comet engulfs Mars: MAVEN observations of comet Siding Spring's
623   influence on the Martian magnetosphere. Geophys. Res. Lett., 42, 8810–8818,
624   doi:10.1002/2015GL066300.
625

626 − Forget, F., Hourdin, F., Fournier, R., Hourdin, C., Talagrand, O., Collins, M., et al. (1999).
627   Improved general circulation models of the Martian atmosphere from the surface to above 80
628   km. Journal of Geophysical Research, 104, 24,155–24,175.
629

630   − Formisano, V., et al., (2005), The Planetary Fourier Spectrometer (PFS) onboard the European
631   Mars Express mission, Planet. Space Sci., 53, 963-974.

632

633   − Giuranna, M., et al., (2017), Preliminary analysis of PFS/MEx observations of Comet Siding
634   Spring, EPSC Abstracts, Vol. 11, EPSC2017-749, 2017

635

636   − Gronoff, G., Rahmati, A., Wedlund, C. S.,Mertens, C. J., Cravens, T. E., & Kallio, E. (2014). The
637   precipitation of keV energetic oxygen ions at Mars and their effects during the comet Siding
638   Spring approach. Geophysical Research Letters, 41, 4844–4850.
639   https://doi.org/10.1002/2014GL060902

640

641   − Gurnett, D. A., et al. (2005), Radar soundings of the ionosphere of Mars, Science, 310, 1929–
642   1933.

643

644   − Gurnett, D.A., Huff, R.L., Morgan, D.D., Persoon, A.M., Averkamp, T.F., Kirchner, D.L., Duru, F.,
645   Akalin, F., Kopf, A.J., Nielsen, E., Safaeinili, A., Plaut, J.J., Picardi, G., (2008). An overview of radar
646   soundings of the martian ionosphere from the Mars Express spacecraft. Adv. Space Res. 41,
647   1335–1346. http://dx.doi.org/10.1016/j.asr.2007.01.062.

648

649   − Gurnett, D. A., Morgan, D. D., Persoon, A. M., Granroth, L. J., Kopf, A. J., Plaut, J. J., and Green, J. L.
650   (2015). An ionized layer in the upper atmosphere of Mars caused by dust impacts from comet
651   Siding Spring. Geophys. Res. Lett., 42, doi:10.1002/ 2015GL063726.

652

653   − Hall, B. E. S., et al. (2016). Annual variations in the Martian bow shock location as observed by
654   the Mars express mission. J. Geophys. Res. Space Physics, 121, doi:10.1002/2016JA023316.

655

656   − Ilyushin, Y. A., Orosei, R., Witasse, O., & Sánchez-Cano, B. (2017). CLUSIM: A synthetic aperture
657   radar clutter simulator for planetary exploration. Radio Science, 52.
658   https://doi.org/10.1002/2017RS006265

659

660   − JPL Small-Body Database: https://ssd.jpl.nasa.gov/sbdb.cgi?ID=dK13A010

661

662   − Kim, S. J., G. S. Orton, C. Dumas, and Y. H. Kim 1996. Infrared spectroscopy of Jupiter's
663   atmosphere after the A and E impacts of Comet Shoemaker–Levy 9. Icarus 120, 326–331.

664

665   −   Kopf, A.J., Gurnett, D.A., Morgan, D.D., Kirchner, D.L., 2008. Transient layers in the topside
666   ionosphere of Mars. Geophys. Res. Lett. 35, 17102. http://dx.doi.org/
667   10.1029/2008GL034948.

669   −   Kopf, A. J., D. A. Gurnett, G. A. DiBraccio, D. D. Morgan, and J. S. Halekas (2017), The transient
670   topside layer and associated current sheet in the ionosphere of Mars, J. Geophys. Res. Space
671   Physics, 122, doi:10.1002/2016JA023591.

673   −   Maurellis, A.N and Cravens, T.E., (2001), Ionospheric Effects of Comet Shoemaker–Levy 9
674   Impacts with Jupiter, *Icarus*, 154, 350–371, doi:10.1006/icar.2001.6709.

676   −   Mendillo, M., G. S. Hawkins and J. A. Klobuchar, A sudden vanishing of the ionospheric F region
677   due to the launch of Skylab, J. Geophys. Res., 80, 2217, 1975

679   −   Mendillo, M., The effect of rocket launches on the ionosphere, Adv. Space Res., 1, 275, 1981.

681   −   Moore, L., J. O'Donoghue, I. Müller-Wodarg, M. Galand, M. Mendillo, (2015), Saturn ring rain:
682   Model estimates of water influx into Saturn's atmosphere, *Icarus,* 245, 355-366,
683   http://dx.doi.org/10.1016/j.icarus.2014.08.041

685   −   Morel, L., O. Witasse, R. Warnant, J.-C. Cerisier, P.-L. Blelly, and J. Lilensten (2004), Diagnostic
686   of the dayside ionosphere of Mars using the total electron content measurement by the
687   NEIGE/Netlander experiment: An assessment study, Planet. Space Sci., 52(7), 603–611,
688   doi:10.1016/j.pss.2003.12.007.

690   −   Morgan, D. D., O. Witasse, E. Nielsen, D. A. Gurnett, F. Duru, and D. L. Kirchner (2013), The
691   processing of electron density profiles from the Mars Express MARSIS topside sounder, Radio
692   Sci., 48, 197–207, doi:10.1002/rds.20023.

694   −   Němec, F., Morgan, D. D., Fowler, C. M., Kopf, A. J., Andersson, L., Gurnett, D. A., Andrews, D. J.,
695   & Truhlik, V. (2017). Ionospheric electron densities at Mars: Comparison of Mars Express
696   ionospheric sounding and MAVEN local measurements. Journal of Geophysical Research:
697   Space Physics, 122, 12,393– 12,405. https://doi.org/10.1002/2017JA024629

699   −   O'Donoghue, J. et al., 2013. The domination of Saturn's low-latitude ionosphere by ring "rain".
700   Nature, 496, (7444), 193–195, http://dx.doi.org/10.1038/nature12049.

702   −   Orosei, R., Jordan, R. L., Morgan, D. D., Cartacci, M., Cicchetti, A., Duru, F., et al. (2015). Mars
703   Advanced Radar for Subsurface and Ionospheric Sounding (MARSIS) after nine years of
704   operation: A summary. Planetary and Space Science, 112, 98–114.
705   https://doi.org/10.1016/j.pss.2014.07.010

706

707   −   Peter, K., et al. (2014), The dayside ionospheres of Mars and Venus: Comparing a one-
708   dimensional photochemical model with MaRS (Mars Express) and VeRa (Venus Express)
709   observations, Icarus, 233, 66–82, doi:10.1016/j.icarus.2014.01.028.

710

711   −   Picardi, G., et al. (2004), MARSIS: Mars advanced radar for subsurface and ionosphere
712   sounding, in Mars Express: The Scientific Payload, ESA Spec. Publ., vol. 1240, edited by A.
713   Wilson and A. Chicarro, pp. 51–69, ESA, Noordwijk, Netherlands

714

715   −   Ramírez-Nicolás, M., B. Sánchez-Cano, O. Witasse, P.-L. Blelly, L. Vázquez, and M. Lester (2016),
716   The effect of the induced magnetic field on the electron density vertical profile of the Mars'
717   ionosphere: A Mars Express MARSIS radar data analysis and interpretation, a case study,
718   Planet. Space Sci., doi:10.1016/j.pss.2016.03.017.

719

720   −   Restano, M., Plaut, J. J., Campbell, B. A., Gim, Y., Nunes, D., Bernardini, F., Egan, A., Seu, R., and
721   Phillips, R. J. (2015). Effects of the passage of Comet C/2013 A1 (Siding Spring) observed by
722   the Shallow Radar (SHARAD) on Mars Reconnaissance Orbiter. Geophys. Res. Lett., 42, 4663–
723   4669, doi:10.1002/2015GL064150.

724
725   −   Russell, C.T., Vaisberg, O., 1983. The interaction of the solar wind with Venus. In: Hunten, D.M.,
726   Colin, L., Donahue, T.M., Moroz, V.I. (Eds.), Venus. The University of Arizona Press, Tuscon, pp.
727   873–940.

728
729   −   Sánchez-Cano, B., O. Witasse,M. Herraiz, S. M. Radicella, J. Bauer, P.-L. Blelly, and G. Rodríguez-
730   Caderot (2012), Retrieval of ionospheric profiles from the Mars Express MARSIS experiment
731   data and comparison with radio-occultation data, Geosci. Instrum. Methods Data Syst., 1, 77–
732   84, doi:10.5194/gi-1-77-2012.

733

734   −   Sánchez–Cano, B., S. M. Radicella, M. Herraiz, O. Witasse, and G. Rodríguez–Caderot (2013),
735   NeMars: An empirical model of the Martian dayside ionosphere based on Mars Express
736   MARSIS data, Icarus, 225, 236–247, doi:10.1016/j.icarus.2013.03.021.

737

738   −   Sánchez–Cano, B., et al. (2015a), Total electron content in the Martian atmosphere: A critical
739   assessment of the Mars Express MARSIS datasets, J. Geophys. Res. Space Physics, 120, 2166–
740   2182, doi:10.1002/2014JA020630.

741

742   −   Sánchez-Cano, B., M. Lester, O. Witasse, S. E. Milan, B. E. S. Hall, P.-L. Blelly, S. M. Radicella, and
743   D. D. Morgan (2015b), Evidence of scale height variations in the Martian ionosphere over the
744   solar cycle, J. Geophys. Res. Space Physics, 120, 10,913–10,925, doi:10.1002/2015JA021949.

745

746   −   Sánchez-Cano, B., et al. (2016a), Solar cycle variations in the ionosphere of Mars as seen by
747   multiple Mars Express data sets, J. Geophys. Res. Space Physics, 121, 2547–2568,
748   doi:10.1002/2015JA022281.2016b

749

750   −   Sánchez-Cano, B., M. Lester, O. Witasse, P.-L. Blelly, M. Cartacci, S.M. Radicella, M. Herraiz, Solar
751   cycle variations in the ionosphere of Mars, (2016b), Física de la Tierra, publication at
752   Department of Physics of the Earth, Astronomy and Astrophysics I of the Universidad
753   Complutense of Madrid, Spain. Vol. 28, 93-108, ISSN: 0214-4557.
754   http://dx.doi.org/10.5209/rev_FITE.2016.v28.53899

755

756   −   Sánchez-Cano, B., et al. (2017). Mars plasma system response to solar wind disturbances
757   during solar minimum. J. Geophys. Res. Space Physics, 122, 6611–6634,
758   doi:10.1002/2016JA023587.

759

760   −   Sánchez – Cano, B., Witasse, O., Lester, M., Rahmati, A., Ambrosi, R., Lillis, R., et al. (2018).
761   Energetic particle showers over Mars from comet C/2013 A1 Siding Spring. Journal of
762   Geophysical Research: Space Physics, 123. https://doi.org/10.1029/2018JA025454

763

764   −   Schleicher, D., Knight, M., & Skiff, B. (2014). Comet C/2013 A1 (Siding Spring). Bureau
765   Electronic Telegrams, 4004, 1.

766

767   −   Schneider, N. M., et al. (2015). MAVEN IUVS observations of the aftermath of the Comet Siding
768   Spring meteor shower on Mars. Geophys. Res. Lett., 42, 4755–4761,
769   doi:10.1002/2015GL063863.

770

771   −   Tricarico, P., et al (2014). Delivery of dust grains from comet C/2013 A1 (Siding Spring) to
772   Mars. Astrophys. J. Lett., 787, L35, doi:10.1088/2041-8205/787/2/L35.

773

774   − Venkateswara Rao, N., ManasaMohana, P., Jayaraman, A., and Rao, S. V. B. (2016), Some new
775   aspects of the transient ionization layer of comet Siding Spring origin in the Martian upper
776   atmosphere. J. Geophys. Res. Space Physics, 121, doi:10.1002/2015JA022189.

777

778   − Vigren, E. and Galand, M. Predictions of Ion Production Rates and Ion Number Densities within
779   the Diamagnetic Cavity of Comet 67P/Churyumov-Gerasimenko at Perihelion. The
780   Astrophysical Journal, 772:33, July 2013. doi: 10.1088/0004-637X/772/1/33.

781

782   − Wang, Y. C., Luhmann, J. G., Rahmati, A., Leblanc, F., Johnson, R. E., Cravens, T. E., & Ip, W. H.
783   (2016). Cometary sputtering of the Martian atmosphere during the Siding Spring encounter.
784   Icarus, 272, 301–308. https://doi.org/10.1016/j.icarus.2016.02.040

785

786   − Witasse, O. et al (2017). Interplanetary coronal mass ejection observed at STEREO-A, Mars,
787   comet 67P/Churyumov-Gerasimenko, Saturn, and New Horizons en route to Pluto:
788   Comparison of its Forbush decreases at 1.4, 3.1, and 9.9 AU. J. Geophys. Res. Space Physics,
789   122, doi:10.1002/2017JA023884.

790

791   − Yelle, R.V., A. Mahieux, S. Morrison, V. Vuitton, S.M. Hörst, (2014), Perturbation of the Mars
792   atmosphere by the near-collision with Comet C/2013 A1 (Siding Spring), Icarus, 237, 202–
793   210, http://dx.doi.org/10.1016/j.icarus.2014.03.030

794